Passivity-Based Inverse Model Predictive Control With Reduced Sensors for Grid-Forming Inverters

Ali Sharida, *Member, IEEE*, Ahmed Kouzou, *Graduate Student Member, IEEE*, Anas Karaki, *Member, IEEE*, Ugur Fesli, *Member, IEEE*, Sertac Bayhan, *Senior Member, IEEE*, and Haitham Abu-Rub, *Fellow, IEEE*

***Abstract*—This article proposes a novel control strategy for grid-forming inverters based on passivity principles and inverse model predictive control (IMPC). The principle of passivity-based control is utilized to reduce the number of required measurements, which enhances the reliability, simplifies the design, and reduces the cost of the control system. Moreover, the proposed approach is generalized to operate reliably even when any group of sensors is unavailable, provided that the other three sensor groups remain available. The sensor groups typically include inverter-side current sensors, filter capacitor voltage sensors, grid-side current sensors, and grid-side voltage sensors. Furthermore, the IMPC technique is employed to control the inverter states effectively, with minimal computational overhead. A key advantage of this approach lies in its ability to generate optimal control signals with a reduced number of sensors, which makes IMPC both optimal and cost-effective. The proposed controller is experimentally validated in multidistributed generation scenarios and is benchmarked against the conventional MPC to demonstrate its effectiveness.**

***Index Terms*—Grid forming inverter, inverse model predictive control (IMPC), passivity-based control, sensorless control.**

I. Introduction

THE global transition toward renewable energy systems (RESs) has fundamentally transformed power system operation paradigm to be more smart. This transition has located the power electronics converters as increasingly vital in many grid's elements such as RESs, electric vehicle charging, and many other evolving smart grid technologies [1]. In addition, conventional synchronous generators are progressively being replaced by inverter-based resources. In this context, grid-forming (GFM) inverters have emerged as a key technology to maintain the stability and reliability of the system [2]. Unlike grid-following inverters, GFM counterparts autonomously establish voltage and frequency references [3], enabling seamless operation under weak grid conditions and in islanded modes. These capabilities are critical for the resilient future power system that is predominantly powered by RESs.

The control of GFM inverters presents unique challenges that have turned significant attention from academic and industry research [4]. These inverters must precisely regulate the magnitude and frequency of voltage [4]. Moreover, they must simultaneously ensure synchronization with other power sources in the network [5]. In addition, proper power sharing among parallel inverter units is critical for system stability [6]. Another critical challenge is maintaining resilience against grid disturbances, which is essential for reliable operation [7]. Furthermore, the control complexity increases when considering additional ancillary services and fault ride-through capability [4].

The GFM inverters require numerous sensors to accomplish these tasks effectively, especially when interfaced with *LCL* filters. The *LCL* filters are preferred over simpler *LC* or *L* filters due to their superior high-frequency harmonic attenuation, which is crucial for complying with grid codes and reducing electromagnetic interference. However, the third-order dynamics of GFM inverters introduce resonance and stability challenges, which often necessitate additional sensors for measuring inverter-side and grid-side currents, as well as filter capacitor voltages. The output voltage is often approximated by the filter capacitor voltage when the output inductance is small. However, explicit measurement becomes important when the inductor impedance is nonnegligible. This improves control accuracy under dynamic and fault conditions. These multifaceted requirements often render existing control approaches inadequate or computationally intensive, posing significant challenges for implementation on low-cost microcontrollers. [8].

Dual loop control structures, which typically employ an inner current control loop and an outer voltage or power control loop, have been widely adopted in power electronic systems due to their simplicity and straightforward implementation [9]. However, these cascaded control architectures suffer from inherent delays between the control loops, which can compromise system performance under dynamic operating conditions. Other

Received 3 June 2025; revised 19 July 2025 and 23 September 2025; accepted 24 October 2025. Date of publication 28 October 2025; date of current version 19 January 2026. This work was supported in part by the Qatar Research, Development, and Innovation (QRDI) under Grant ARG01-0428-230023. Recommended for publication by Associate Editor H. Wu. *(Corresponding author: Ali Sharida.)*

Ali Sharida and Anas Karaki are with Qatar Environment and Energy Research Institute, Hamad Bin Khalifa University, Doha 34110, Qatar (e-mail: asharida@hbku.edu.qa; akaraki@hbku.edu.qa).

Ahmed Kouzou is with the Department of Electrical and Computer Engineering, Texas A&M University, TX 77843 USA (e-mail: ahmed.kouzou@tamu.edu).

Ugur Fesli is with the Department of Electrical & Electronic Engineering, Gazi University, Ankara 06560, Türkiye (e-mail: ugurfesli@gazi.edu.tr).

Sertac Bayhan is with Qatar Environment and Energy Research Institute, Hamad Bin Khalifa University, Doha 34110, Qatar, and also with the Department of Electrical & Electronic Engineering, Gazi University, Ankara 06560, Türkiye (e-mail: sbayhan@hbku.edu.qa).

Haitham Abu-Rub is with the College of Science and Engineering (CSE), Hamad Bin Khalifa University, Doha 5825, Qatar (e-mail: habu-rub@hbku.edu.qa).

Color versions of one or more figures in this article are available at https://doi.org/10.1109/TPEL.2025.3626253.

Digital Object Identifier 10.1109/TPEL.2025.3626253

conventional linear control methods often fall short in meeting multiple control objectives at the same time. In response to these limitations, researchers have developed increasingly sophisticated control algorithms. Among the advanced techniques proposed to address these challenges are methods such as: sliding mode control (SMC), which offers improved robustness and dynamic performance. Samanta et al. [10], direct power control [11], fuzzy logic control [7], Lyapunov-based control [12], passivity based control [13], and linear quadratic trackers [14]. Each methodology offers distinct advantages and targets specific aspects of the control problem. However, they also exhibit significant limitations, especially when applied to applications with GFM inverter. SMC often suffers from chattering phenomena that can stress power electronic components [15]. Direct power control may struggle with transient performance during rapid load changes as it represents a single-input single-output control system [15]. Fuzzy logic controllers require extensive tuning, lack theoretical stability guarantees, and lack systematic methodologies to design input–output rules and memberships [15]. Lyapunov-based strategies guarantee the global stability of the control system but lack the ability to achieve optimal and a predefined characteristics. Moreover, passivity based controllers can guarantee global stability, but lacks the ability to regulate the states in a predefined manner. Finally, linear quadratic approaches perform well in linear systems but its performance degrades with system nonlinearities.

On the other hand, model predictive control (MPC) has attracted significant attention among various control strategies in power electronics applications [16], [17], primarily due to its inherent capability to handle multiple objectives and constraints simultaneously. MPC utilizes a dynamic model to predict future system behavior, then optimizes control actions according to a predefined cost function. This offers exceptional advantages for GFM inverter applications including flexibility, optimal performance, the ability to address multiple objectives, handle system nonlinearities, and satisfy various operational constraints. Moreover, MPC can operate without a dedicated pulsewidth modulation stage, which simplifies the control architecture. Despite its numerous advantages, the practical implementation of MPC is hindered by a significant challenge which is its high computational burden. This computational intensity arises from the need to evaluate all possible switching combinations in every control cycle to determine the optimal control action. For three-phase inverter, there are numerous switching combinations (3^N, N: number of levels), each must be assessed through state prediction and cost function calculation. This computational demand becomes prohibitive in real-world applications, particularly when low-cost microcontrollers are used, as they are incapable of handling such intensive processing—especially when combined with additional GFM functionalities such as ancillary services.

The challenge of balancing computational efficiency with control performance remains a critical concern, particularly in GFM inverter applications. To address this, the principle of inverse model predictive control (IMPC) has gained increasing attention, as it offers a promising compromise between real-time control performance and computational efficiency [18], [19]. In power electronics, the IMPC was first proposed in [20] for grid following inverters, then it was extended for various applications such as EV chargers [21], dual active bridge converters [22], and multiport solid state transformers [23]. However, none of the existing studies have addressed GFM inverters, which require more advanced control strategies due to their roles in voltage and frequency regulation. Furthermore, these works have overlooked the distinctive multisensor requirements of GFM inverters and have not proposed any approaches to reduce the number of required sensors. This gap is particularly critical, as GFM inverters rely on numerous measurements to achieve voltage regulation, frequency control, and stable interfacing through *LCL* filters.

To reduce reliance on physical sensors, numerous sensorless control techniques have been proposed, including Kalman filters [24], state feedback observers [25], Luenberger observers [26], and sliding mode observers [27]. However, these methods are typically tailored to estimate specific states or sensor signals, and their observer configurations must be manually redesigned if a different set of sensors becomes unavailable. In dynamic operating environments, where sensors are susceptible to faults or disconnections, such inflexibility becomes a critical limitation. This highlights the growing need for adaptive and reconfigurable observer architectures capable of autonomously adjusting to changing sensor availability, while maintaining accurate state estimation without necessitating controller redesign.

This article proposes a control mechanism that leverages the simplicity of IMPC along with the robustness of passivity-based design. Due to its low computational burden, IMPC facilitates the integration of additional functionalities, such as sensor count reduction, without increasing algorithm complexity. In addition, the method proposed in this work provides a flexible architecture that can autonomously reconfigure itself to estimate any missing sensor signal, without the need for controller redesign. This adaptability makes it particularly suitable for dynamic and fault-prone environments where sensor availability cannot be guaranteed. This makes the approach especially suitable for modern GFM inverter applications, where compact, reliable, and cost-effective control implementations are essential. Finally, the contributions of this article are summarized as follows:

1) An optimal passivity-based IMPC approach is proposed for GFM-inverters.
2) Proposing an approach that offers a flexibility to eliminate any sensor, whether at the grid side, within the filter, or on the inverter side.
3) Introducing tuning-free control which features reduced computational requirements.
4) The proposed approach can achieve multiple-objectives, handle system nonlinearities, and is compatible with low-cost microcontrollers.

II. GFM Inverter Dynamic Model

The circuit diagram of the GFM inverter is shown in Fig. 1. The dynamic model of a three-phase GFM inverter with *LCL* filter contains three controlled states, grid side current (i_o), filter capacitor voltage (v_c), and inverter current (i_i). These states are

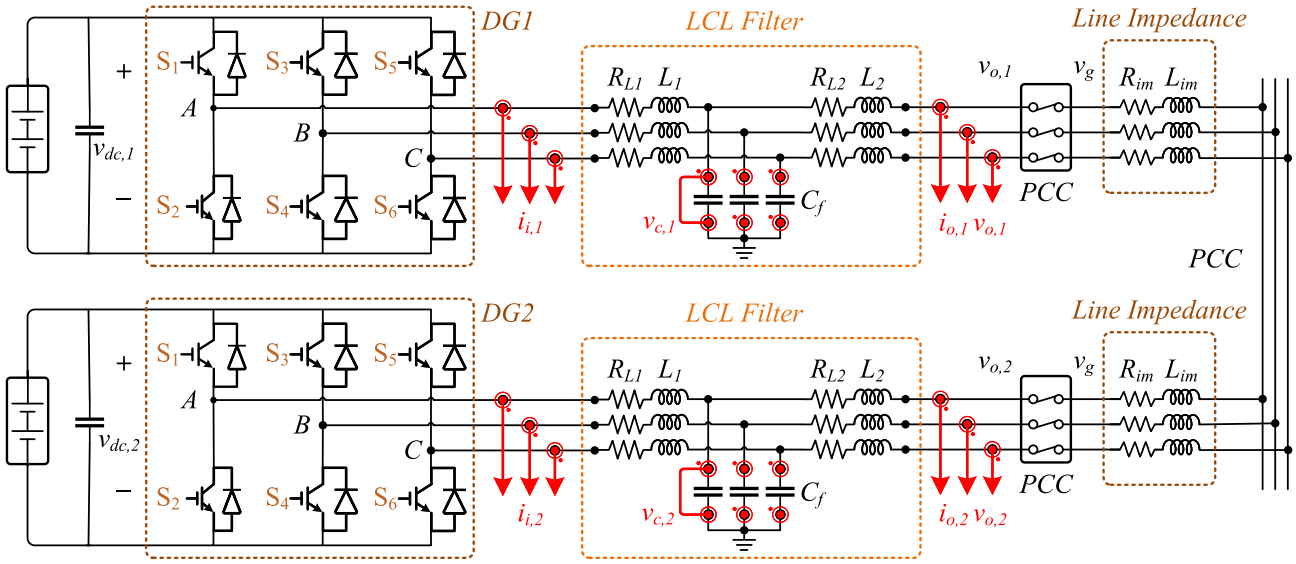

Fig. 1. Circuit diagram of GFM inverter with *LCL* filter.

regulated through inverter's voltage (v_i) as follows [28]:

$$\frac{di_i}{dt} = \frac{-R_i}{L_i} i_i - \frac{1}{L_i} v_c + \frac{1}{L_i} v_i \tag{1}$$

$$\frac{dv_c}{dt} = \frac{1}{C_f} i_i - \frac{1}{C_f} i_o \tag{2}$$

$$\frac{di_o}{dt} = \frac{1}{L_o} v_c - \frac{R_o}{L_o} i_o - \frac{1}{L_o} v_o \tag{3}$$

where R_i and L_i are the resistance and inductance of the input inductor, R_o and L_o are the resistance and inductance of the output inductor, C_f is the capacitance of the *LCL* filter, and v_o is the output voltage after the filter.

Equations (1)–(3) can be written in the vector form as follows:

$$\dot{x} = Ax + Bv_{i,\alpha\beta} + Cv_{o,\alpha\beta} \tag{4}$$

where x is the state vector $\begin{bmatrix} i_{i,\alpha\beta} & v_{c,\alpha\beta} & i_{o,\alpha\beta} \end{bmatrix}^T$, $\dot{x}$ is the derivative of the state vector, and the A, B, and C are the input and output matrices and can be represented by

$$A = \begin{bmatrix} -\frac{R_i}{L_i} & -\frac{1}{L_i} & 0 \\ \frac{1}{C_f} & 0 & -\frac{1}{C_f} \\ 0 & \frac{1}{L_o} & -\frac{R_o}{L_o} \end{bmatrix} \tag{5}$$

$$B = \begin{bmatrix} \frac{1}{L_i} \\ 0 \\ 0 \end{bmatrix} \tag{6}$$

$$C = \begin{bmatrix} 0 \\ 0 \\ -\frac{1}{L_o} \end{bmatrix}. \tag{7}$$

Equation (4) can be discretized using Du Hamel integral approach [29]

$$x(k+1) = A_k x(k) + B_k v_{i,\alpha\beta}(k) + C_k v_{o,\alpha\beta}(k) \tag{8}$$

where

$$x(k) = \begin{bmatrix} i_{i,\alpha}(k) & i_{i,\beta}(k) \\ v_{c,\alpha}(k) & v_{c,\beta}(k) \\ i_{o,\alpha}(k) & i_{o,\beta}(k) \end{bmatrix} \in \mathbb{R}^{3\times 2}$$

$$A_k = e^{AT_s}$$

$$B_k = A^{-1}(A_k - I_{3\times 3})B$$

$$C_k = A^{-1}(A_k - I_{3\times 3})C. \tag{9}$$

III. Passivity-Based State Estimation Design

This section presents an adaptive approach for estimating the complete state vector of the system given any three measurement vectors. The full measurements vector (z_k) to be estimated is defined as

$$z = \begin{bmatrix} i_{i,\alpha\beta} & v_{c,\alpha\beta} & i_{o,\alpha\beta} & v_{o,\alpha\beta} \end{bmatrix}^T \in \mathbb{R}^{4\times 2}. \tag{10}$$

The estimation procedure assumes that any three of these four measurement vectors are available at any given time. Depending on which three measurement vectors are available, different estimation equations for the missing vector are derived.

First, if $v_{o,\alpha\beta}$, $i_{o,\alpha\beta}$, and $v_{c,\alpha\beta}$ are available, the input current $i_{i,\alpha\beta}$ can be estimated as [28]:

$$\hat{i}_{i,\alpha\beta} = i_{o,\alpha\beta} - \omega_g C_f J v_{c,\alpha\beta} \tag{11}$$

where J is the skew matrix and is given by

$$J = \begin{bmatrix} 0 & -1 \\ 1 & 0 \end{bmatrix}. \tag{12}$$

Second, if $v_{o,\alpha\beta}$, $i_{o,\alpha\beta}$, and $i_{i,\alpha\beta}$ are available, the capacitor voltage v_c can be estimated as

$$\hat{v}_{c,\alpha\beta} = v_{o,\alpha\beta} - \omega_g L_o J i_{o,\alpha\beta}. \tag{13}$$

Third, if $v_{o,\alpha\beta}$, $v_{c,\alpha\beta}$, and $i_{i,\alpha\beta}$ are available, the output current $i_{o,\alpha\beta}$ can be estimated using

$$\hat{i}_{o,\alpha\beta} = \frac{1}{\omega_g L_o} J^T (v_{o,\alpha\beta} - v_{c,\alpha\beta}). \tag{14}$$

Finally, if $i_{o,\alpha\beta}$, $v_{c,\alpha\beta}$, and $i_{i,\alpha\beta}$ are available, the output voltage $v_{o,\alpha\beta}$ can be computed by

$$\hat{v}_{o,\alpha\beta} = v_{c,\alpha\beta} + \omega_g L_o J i_{o,\alpha\beta}. \tag{15}$$

To create a complete and consistent state estimate, an availability indicator matrix (C_x) is introduced that selectively combines measured and estimated values as follows:

$$C_x = \begin{bmatrix} c_{ii} & c_{vc} & c_{io} & c_{vo} \end{bmatrix}^T, \quad c_i \in \{0, 1\} \tag{16}$$

where each c_i indicates whether the corresponding measurement vector is available ($c_i = 1$) or not ($c_i = 0$). The values of c_i can be dynamically set based on sensor fault detection and localization techniques, as discussed in [30].

Finally, the estimated state vector can be explicitly presented as

$$\hat{z}(k) = C_x \circ z(k) + (1_{4\times1} - C_x) \circ \hat{z}_{est} \tag{17}$$

where $\hat{z}_{est}$ represents the estimation results obtained from (11) to (15), and $\hat{z}$ is a vector combines the known measurement vectors combined with the estimation of the unknown one. The symbol ($\circ$) refers to elementwise scalar-vector multiplication, and $1_{4\times1}$ is vector of all ones.

However, a key limitation of this approach that it assumes accurate knowledge of system parameters L_o, L_i, and C_f. However, in practical applications, these parameters often contain uncertainties due to manufacturing tolerances, temperature variations, and aging effects. A straightforward approach to address parameter uncertainties is the online estimation correction based on the error between the available measurement vectors and their estimates. The key insight is that parameter uncertainties affect both the known and unknown vectors in a systematic manner. This allows the error patterns of available measurement vectors to improve the accuracy of the estimation. Therefore, passivity-based control is proposed to regulate the convergence of estimation error.

Using (10), the dynamic model of (8) can be converted into an augmented state-space model as follows:

$$z(k+1) = A_z(k) z(k) + B_z(k) v_{i,\alpha\beta}(k) \tag{18}$$

with

$$A_z(k) = \begin{bmatrix} A_k & C_k \\ 0 & I \end{bmatrix}, \quad B_z(k) = \begin{bmatrix} B_k \\ 0 \end{bmatrix}. \tag{19}$$

Let $e_z(k)$ represents the error of $z(k)$ estimation,

$$e_z(k) = C_x \circ (z(k) - \hat{z}(k). \tag{20}$$

Accordingly, the error at the next time step is given by

$$e_z(k+1) = C_x \circ (z(k+1) - \hat{z}(k+1)). \tag{21}$$

For the estimated measurement $\hat{z}$ to be an equilibrium point ($z(k) = \hat{z}(k)$) under the control input $v_{i,\alpha\beta}$, the following condition must be satisfied:

$$\hat{z}(k+1) = A_z z(k) + B_z v_{i,\alpha\beta}(k). \tag{22}$$

To ensure this condition will be satisfied, define a storage function (discrete-time energy function) as follows:

$$H(e_z) = \frac{1}{2} e_z^T I_{4\times4} e_z \tag{23}$$

where $I_{4\times4}$ is 4×4 identity matrix. Then, the change in error energy between two consecutive time steps is

$$\Delta H(k) = H(e_z(k+1)) - H(e_z(k)) \tag{24}$$

$$= \frac{1}{2} e_z(k+1)^T I_{4\times4} e_z(k+1) - \frac{1}{2} e_z(k)^T I_{4\times4} e_z(k). \tag{25}$$

To ensure the system's energy decreases over time, add the damping injection as a correction signal (ζ) to the estimation process as follows:

$$\hat{z}(k+1) = A_z \hat{z}(k) + B_z v_{i,\alpha\beta}(k) + \zeta. \tag{26}$$

Substituting (26) into (21), the dynamics of the estimation error becomes

$$e_z(k+1) = A_z e_z(k) - \zeta. \tag{27}$$

Let the damping rejection signal ζ to be defined as

$$\zeta = K_z e_z(k) \tag{28}$$

where K_z is a feedback gain matrix. After substituting the damping rejection signal, the energy function becomes

$$\Delta H(k) = \frac{1}{2} C_x (z(k) - \hat{z}(k))^T * \big((A_z - K_z)^T I_{4\times4} (A_z - K_z) - I_{4\times4}\big) * C_x (z(k) - \hat{z}(k)). \tag{29}$$

To achieve the passivity condition, the energy of the error must be decreased with respect to a specific supply rate. The supply rate is selected to be the product between the system's input and output. Where the input of the observer is the applied damping signal ($\zeta = K_z e_z(k)$), and the output is the estimation error ($e_z(k)$). Let the supply rate (S_R)to be defined as

$$S_R = u^T y = \zeta e_z(k). \tag{30}$$

The passivity condition becomes

$$\Delta H(k) <= S_R. \tag{31}$$

Therefore,

$$\frac{1}{2} e_z(k)^T \left((A_z - K_z)^T I_{4\times4} (A_z - K_z) - I_{4\times4}\right) e_z(k) <= \zeta e_z(k). \tag{32}$$

After some mathematical manipulation of (32), K_z must satisfy the following inequality to ensure dissipativity:

$$\frac{1}{2} (A_z - K_z)^T I_{4\times4} (A_z - K_z) - K_z <= I_{4\times4}. \tag{33}$$

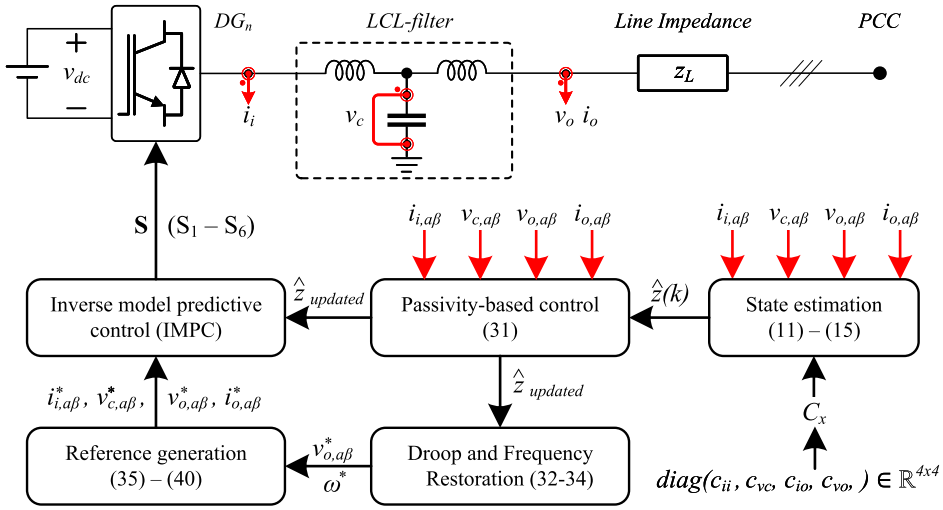

Fig. 2. Control block diagram.

Finally, the updated estimation vector ($\hat{z}_{\text{updated}}$) can be defined explicitly as

$$\hat{z}_{\text{updated}} = C_x \circ \hat{z}_k + (1_{4\times1} - C_x) \circ \hat{z}_{est} + K_z e_z(k). \quad (34)$$

IV. Proposed Control Approach

The proposed control block diagram is shown in Fig. 2. It consists of two subsystems including reference signal generation and IMPC for states regulation. These subsystems will be discussed in the following sections.

A. Reference Signal Generation

The operation of GFM inverters is typically governed by a combination of control strategies, such as droop control, frequency restoration, and virtual impedance, which collectively enable decentralized operation, proportional power sharing, and system stability.

Droop control is a primary mechanism that enables autonomous load sharing among parallel inverters without requiring communication links. This can be achieved by adjusting the inverter's frequency and voltage based on deviations in active and reactive power from their respective setpoints as follows:

$$\begin{aligned} \omega^* &= \omega^*_{\text{nominal}} - k_P(P - P^*) \\ v^*_{o,\text{droop}} &= v^*_{o,\text{nominal}} - k_Q(Q - Q^*) \end{aligned} \quad (35)$$

where $\omega^*_{\text{nominal}}$ and $v^*_{o,\text{nominal}}$ represent the nominal frequency and voltage references, P and Q are the measured active and reactive output powers, P^* and Q^* are their respective setpoints, and k_P, k_Q are the droop coefficients that determine the sensitivity of the response and how the power is shared proportionally.

However, standard droop control results in steady-state frequency deviations as a result of its open-loop nature. To mitigate this, a secondary control loop is introduced for frequency restoration to offset the generated frequency reference ω^* from (35)

$$\Delta\omega^*_{\text{res}} = k_P(\omega - \omega^*_{\text{nominal}}) + k_I \int (\omega - \omega^*_{\text{nominal}})\, dt. \quad (36)$$

In this expression, k_P and k_I are the proportional and integral gains. This mechanism ensures that the frequency deviation is eliminated over time, which enables the system to restore its nominal operating frequency.

Furthermore, virtual impedance is incorporated to emulate desirable impedance characteristics at the inverter's output. This is essential for improving stability margins and ensuring equitable power sharing among parallel inverters with different line impedances. This action can be achieved as follows:

$$v^*_o = v^*_{o,\text{droop}} - Z_{\text{virt}} \cdot i_o \quad (37)$$

where, v^*_o is the final voltage reference used for modulation, Z_{virt} is the virtual output impedance (commonly expressed as $R + j\omega L$), and i_o is the inverter output current. These three strategies—droop control, frequency restoration, and virtual impedance—are integrated to generate robust reference signals for frequency and voltage. These references are then tracked precisely by the IMPC.

B. IMPC Design

In GFM, only inverter current ($i_{i,\alpha\beta}$) has a direct relation with control signal ($v_{i,\alpha\beta}$). Therefore, the reference voltage is first transformed into output current reference ($i^*_{o,\alpha\beta}$), then into capacitor voltage reference ($v^*_{c,\alpha\beta}$), and finally into inverter current reference ($i^*_{i,\alpha\beta}$). Starting from the active and reactive powers (P and Q), they are represented as

$$\begin{aligned} P(k+1) = 1.5\,[&v_{o,\alpha}(k+1)i_{o,\alpha}(k+1) \\ &+ v_{o,\beta}(k+1)i_{o,\beta}(k+1)] \end{aligned} \quad (38)$$

$$\begin{aligned} Q(k+1) = 1.5\,[&v_{o,\beta}(k+1)i_{o,\alpha}(k+1) \\ &- v_{o,\alpha}(k+1)i_{o,\beta}(k+1)]\,. \end{aligned} \quad (39)$$

By solving (40), the unsaturated output current reference ($I^*_{o,\alpha\beta}$) can be obtained by

$$I^*_{o,\alpha} = \frac{2}{3} \cdot \frac{P \cdot v^*_{o,\alpha} + Q \cdot v^*_{o\beta}}{v^{*2}_{o,\alpha} + v^{*2}_{o,\beta}} \tag{40}$$

$$I^*_{o,\beta} = \frac{2}{3} \cdot \frac{P \cdot v^*_{o,\beta} - Q \cdot v^*_{o,\alpha}}{v^{*2}_{o,\alpha} + v^{*2}_{o,\beta}}. \tag{41}$$

However, it is crucial to achieve current limiting during critical situations in GFM applications [31]. Therefore, saturated reference current components can be written as

$$\begin{bmatrix} i^*_{o,\alpha} \\ i^*_{o,\beta} \end{bmatrix} = \min\left(1, \frac{\sqrt{2} \cdot i_{o,\max}}{\sqrt{i^{*2}_{o,\alpha} + i^{*2}_{o,\beta}}}\right) \cdot \begin{bmatrix} I^*_{o,\alpha} \\ I^*_{o,\beta} \end{bmatrix}. \tag{42}$$

Using (42), the reference capacitor voltage is obtained by [3], [8], [28]

$$\begin{aligned} v^*_{c,\alpha} &= v^*_{o,\alpha} - \omega_g L_o i^*_{o,\beta} \\ v^*_{c,\beta} &= v^*_{o,\beta} + \omega_g L_o i^*_{o,\alpha}. \end{aligned} \tag{43}$$

Then, based on (43), the reference capacitor voltage is then transformed to the inverter side current by

$$\begin{aligned} i^*_{i,\alpha} &= i^*_{o,\alpha} - \omega_g C_f v^*_{c,\beta} \\ i^*_{i\beta} &= i^*_{o,\beta} + \omega_g C_f v^*_{c,\alpha}. \end{aligned} \tag{44}$$

It is worth noting that the ω-coupling terms in (43) and (44) arises from the time derivative of sinusoidal $\alpha\beta$ components.

As all references are generated, the IMPC can be designed by introducing a multiobjective cost function. The general formula of a GFM cost function can be represented by

$$\begin{aligned} g = &(i^*_{i,\alpha\beta} - i_{i,\alpha\beta}(k+1))^2 + (v^*_{c,\alpha\beta} - v_{c,\alpha\beta}(k+1))^2 \\ &+ (i^*_{o,\alpha\beta} - i_{o,\alpha\beta}(k+1))^2. \end{aligned} \tag{45}$$

The weights in the cost function are set equally to prioritize all controlled states uniformly and simplify controller design by avoiding complex tuning. Alternative weighting schemes can be applied systematically to balance performance tradeoffs, as shown in [32].

The objective of the IMPC is to minimize g to fulfill the GFM control requirements. The most optimal value of the cost function is $g = 0$. This value can be achieved if

$$\begin{aligned} i^*_{i,\alpha\beta} &\approx i_{i,\alpha\beta}(k+1) \\ v^*_{c,\alpha\beta} &\approx v_{c,\alpha\beta}(k+1) \\ i^*_{o,\alpha\beta} &\approx i_{o,\alpha\beta}(k+1). \end{aligned} \tag{46}$$

These conditions can be represented in vector form as

$$x(k+1) = x^* = \begin{bmatrix} i^*_{i,\alpha\beta} \\ v^*_{c,\alpha\beta} \\ i^*_{o,\alpha\beta} \end{bmatrix}. \tag{47}$$

Then, substitute (47) in (8), the state space representation becomes

$$x^* = A_k x(k) + B_k v_{i,\alpha\beta}(k) + C_k v_{o,\alpha\beta}(k). \tag{48}$$

Equation (48) can be written as a function of the control signal as follows:

$$v_{i,\alpha\beta}(k) = B_k^{-1}\left[x^* - A_k x(k) - C_k v_{o,\alpha\beta}(k)\right]. \tag{49}$$

However, the challenge in this stage is computing B_k^{-1}. B_k^{-1} is required to enable the IMPC to optimize the control signal, but B_k^{-1} is not square. To overcome this design step, the inverse vector is approximated using Moore–Penrose pseudo-inverse as follows [33]:

$$B_k^{-1} = (B_k^T B)^{-1} B_k^T. \tag{50}$$

Although (50) contains matrix operations which require high computational burden, B_k is constant. Therefore, B_k^{-1} is constant too, which means B_k^{-1} can be computed offline and located numerically in (49). Based on (49) and (50), the formula of the IMPC becomes

$$v_{i,\alpha\beta}(k) = (B_k^T B)^{-1} B_k^T \left[x^* - A_k x(k) - C_k v_{o,\alpha\beta}(k)\right] \tag{51}$$

and for sensorless control, the IMPC formula becomes

$$v_{i,\alpha\beta}(k) = (B_k^T B)^{-1} B_k^T \left[x^* - A_k \hat{x}(k) - C_k \hat{v}_{o,\alpha\beta}(k)\right] \tag{52}$$

where $\hat{x}(k)$ is a subset vector of $\hat{z}(k)$, and given by

$$\hat{x}(k) = \begin{bmatrix} \hat{i}_{i,\alpha\beta} \\ \hat{v}_{c,\alpha\beta} \\ \hat{i}_{o,\alpha\beta} \end{bmatrix}. \tag{53}$$

From (52), it can be noticed that the output voltage regulation and current shaping are simultaneously achieved within a unified predictive control law. This eliminates the need for explicit current reference generation and separate tracking loops, thereby simplifying the control structure and avoiding loop interaction issues. In addition, the proposed single-loop IMPC inherently incorporates the full *LCL* filter dynamics in its prediction model. As a result, the control action directly considers and damps the resonance modes without relying on auxiliary damping controllers or bandwidth separation. Furthermore, the absence of cascaded loops eliminates additional control delays, which ensures a fast and coordinated response that enhances overall system stability.

V. Stability Analysis

To analyze the stability of the proposed control approach, substitute the control law (51) into the system dynamics (8)

$$\begin{aligned} x(k+1) = &\left[A_k - B_k(B_k^T B_k)^{-1} B_k^T A_k\right] x(k) \\ &+ \left[I - B_k(B_k^T B_k)^{-1} B_k^T\right] C_k v_{o,\alpha\beta}(k) \\ &+ B_k(B_k^T B_k)^{-1} B_k^T x^*. \end{aligned} \tag{54}$$

For simplicity, let $M = B_k(B_k^T B_k)^{-1} B_k^T$, then the closed-loop system can be simplified to

$$x(k+1) = (I - M)A_k x(k) + (I - M)C_k v_{o,\alpha\beta}(k) + M x^*. \tag{55}$$

To analyze asymptotic stability, a special focus on the homogeneous system is considered by setting both the reference and

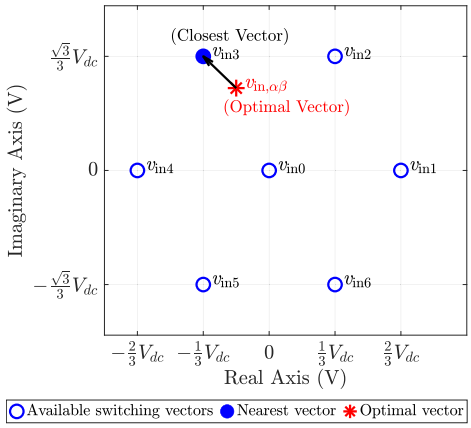

Fig. 3. Closest voltage vector selection.

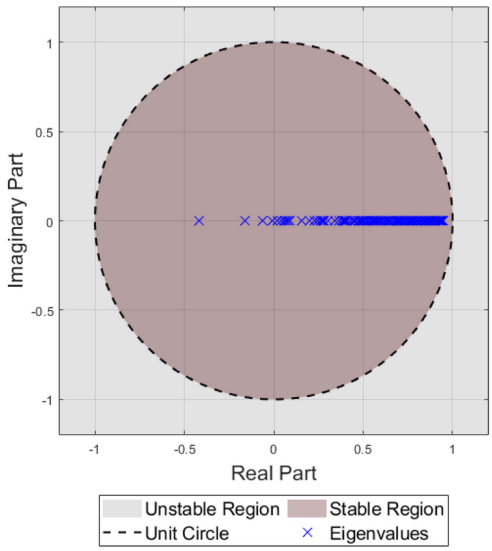

Fig. 4. Eigenvalues of the closed loop control with passive parameters sweeping.

the external input to zeros. This simplifies the system to

$$x^* = 0, \quad v_{o,\alpha\beta}(k) = 0. \tag{56}$$

This leads to the following homogeneous system:

$$x(k+1) = (I - M)A_k x(k). \tag{57}$$

The homogeneous system is asymptotically stable if the state $x(k)$ converges to zero as $k \to \infty$. This occurs if all eigenvalues λ_i of the matrix $(I - M)A_k$ satisfy the following conditions:

$$|\lambda_i| < 1. \tag{58}$$

The eigenvalues of (57) are obtained by sweeping the passive parameters L_i, L_o, R_i, R_o, and C_f for a wide range. The inductors are swept in the range 1 to 10 mH, the resistances are swept in the range $10\,m\Omega$ to $0.1\,\Omega$, and the capacitance is swept between 10 to 50 μF and the eigenvalues are collected and plotted inside a unit circle as shown in Fig. 4. It can be noticed that all eigenvalues are located inside a unit circle which satisfies $|\lambda_i| < 1$, thus, the system is asymptotically stable.

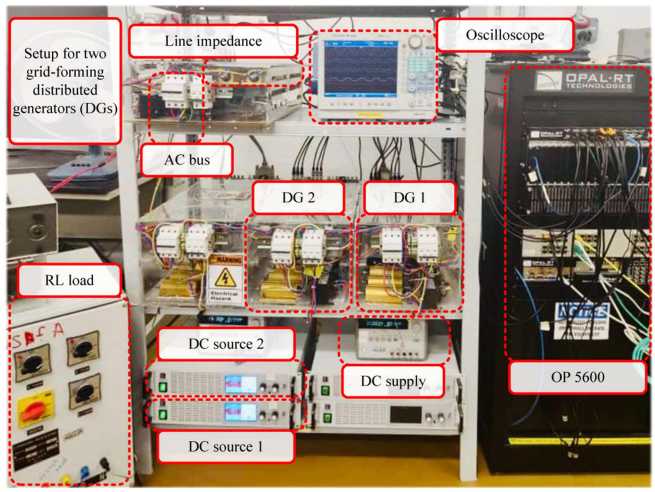

Fig. 5. Experimental microgrid setup with two DGs.

TABLE I
PHYSICAL PARAMETERS USED IN THE EXPERIMENTAL SETUP

Components	DG_1	DG_2
Input Inductor L_i	2.8 mH	2.7 mH
DC Resistance of L_i	0.2 Ω	
Filter Capacitor C_f	25 μF	
Output Inductor L_o	0.9 mH	1 mH
DC Resistance of L_o	0.15 Ω	
Impedance Line Resistance R_{line}	1 Ω	1.1 Ω
Impedance Line Inductance L_{line}	0.16 mH	
DC Voltage Source	250 V	
Rated power	4 kW	3 kW

VI. EXPERIMENTAL RESULTS

The proposed control algorithm is implemented on the OPAL-RT OP5600 to control a two-DG microgrid. Each DG consists of a three-phase two-level inverter powered by a dc supply. Each inverter is connected to the ac bus through an *LCL* filters followed by an RL line impedance. The experimental setup is depicted in Fig. 5, and the system parameters used are listed in Table I.

The controller is then tested under four sensorless scenarios, as shown in Fig. 6. These scenarios include: a) capacitor voltage sensorless control, b) output voltage sensorless control, c) output current sensorless control, and d) input current sensorless control. In the first three cases, the controller maintains performance nearly identical to the fully sensored configuration, and achieves excellent voltage and current regulation. However, in the absence of input current measurements, the quality of the DG currents degrades, and power sharing becomes inaccurate. This degradation occurs because the input current is the only variable that has a direct relation to the computation of the control signal $v_{i,\alpha\beta}$.

Despite this limitation, sensorless input current control remains valuable in the context of fault-tolerant operation. In practical applications, sensor faults are common and can compromise system stability if not handled appropriately. The proposed control strategy demonstrates a high degree of robustness and adaptability in degraded sensing conditions. Specifically, in the

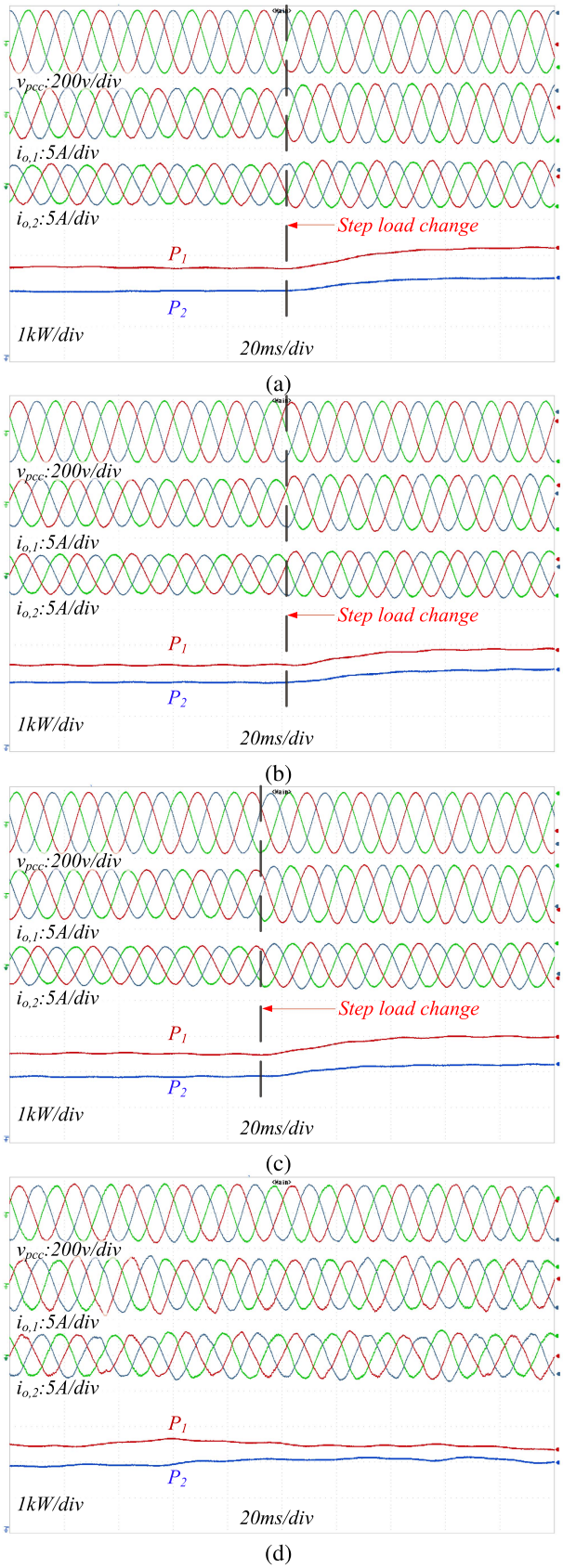

Fig. 6. Sensorless control results. (a) v_c sensor-less control, (b) i_o sensor-less control, (c) v_o sensor-less control, and (d) i_i sensor-less control.

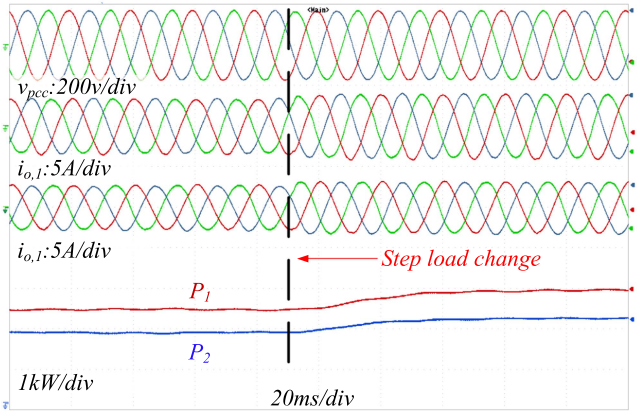

Fig. 7. v_c sensorless control with 10% passive parameters uncertainty.

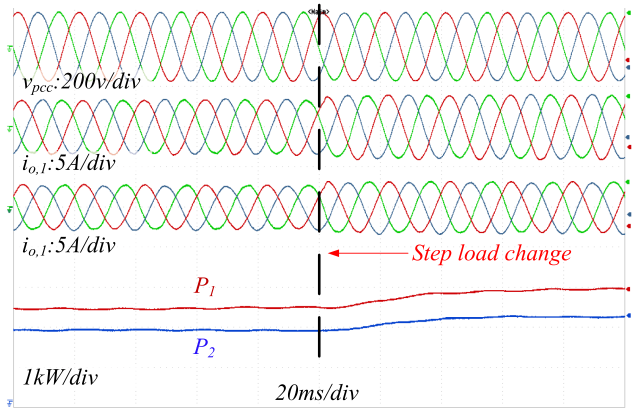

Fig. 8. i_o sensorless control with 20% change in line impedance.

first three sensorless scenarios, where capacitor voltage, output voltage, or output current measurements are eliminated, the controller continues to deliver excellent dynamic and steady-state performance, nearly identical to the fully sensored case. This confirms the effectiveness of the passivity-based design in minimizing sensing requirements without sacrificing control quality. Even in the most challenging case, where input current measurements are unavailable, the system maintains stable operation, though with some degradation in current quality and power sharing.

Nevertheless, from a design and cost-optimization perspective, it is recommended to retain the input current sensors while eliminating any of the other sensor groups, such as the capacitor voltage sensors, output current sensors, or output voltage sensors depending on the specific application requirements.

Fig. 7 shows the response of the proposed control technique with the absence of v_c measurements and the passive parameters (L_i, C_f, L_o) has 10% uncertainty. The uncertainty is intentionally added to the parameters by multiplying each parameter by 0.9 inside the control and observer loops. The results show that the response maintains sinusoidal currents, and around zero steady-state error. This validates the robustness of the proposed

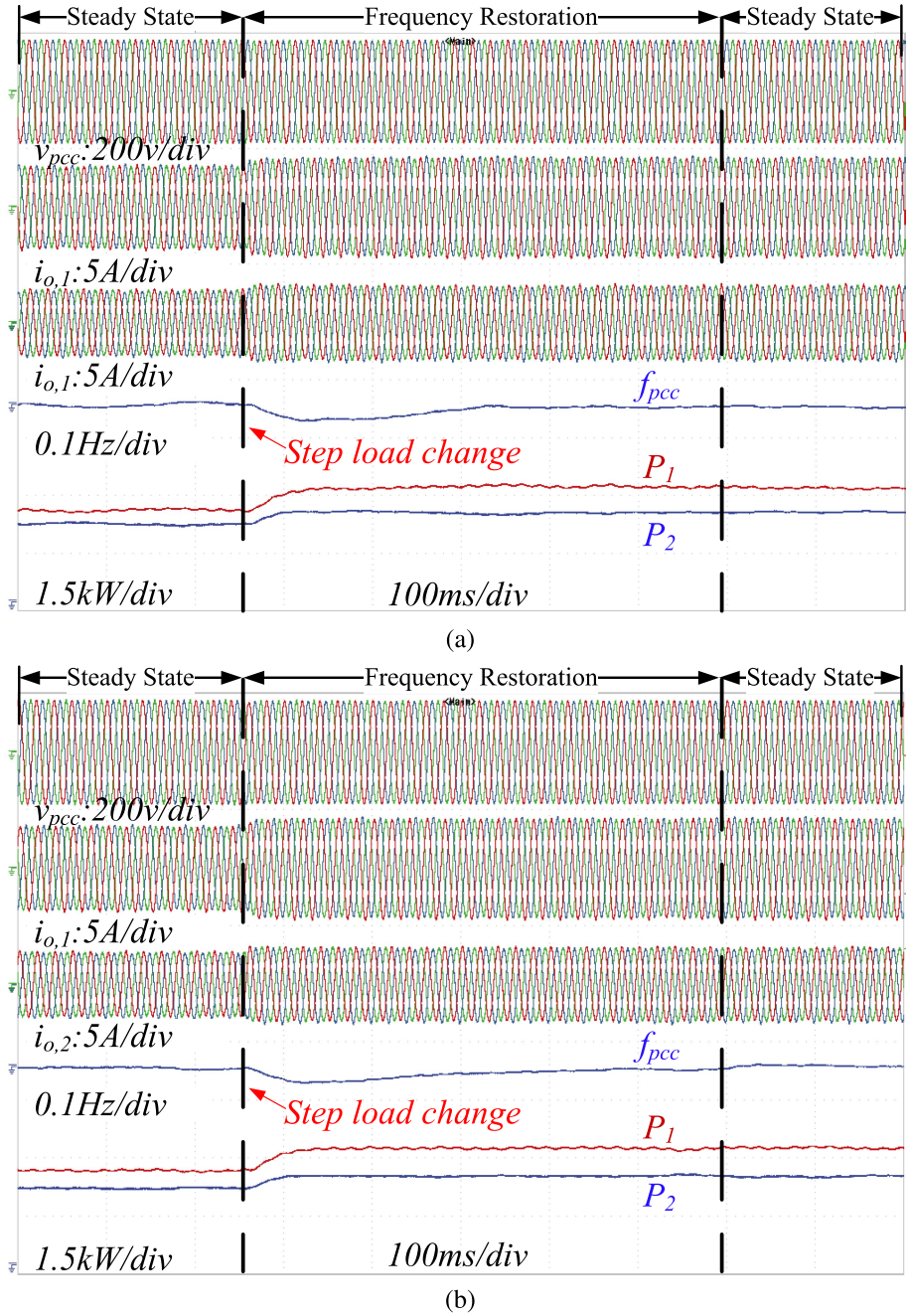

Fig. 9. Comparison analysis (a) PB-IMPC response with $v_{o,\alpha\beta}$ sensorless control and (b) Conventional MPC response with full set of sensors.

method against passive parameters variation, and its ability to estimate the missing measurements even when uncertainties exist.

Fig. 8 shows the response of the proposed control technique with the absence of i_o measurements under a stronger grid scenario. The grid strength is increased by reducing the line impedance by 20%, which results in a lower output impedance seen by the inverter. The controller and observer remain unchanged. The results demonstrate that the system maintains sinusoidal current waveforms and exhibits negligible steady-state error, which validates the robustness of the proposed method in stronger grid conditions.

Fig. 9 illustrates the PCC voltage, DG currents, frequency response, and power outputs of the DGs under two control strategies 1) the proposed PB-IMPC operating without output voltage measurements, and 2) conventional MPC with full sensor availability, respectively. Despite the reduced sensing, the PB-IMPC controller achieves voltage and current regulation performance that closely matches that of the full-sensor MPC. Upon a step load change, both controllers exhibit appropriate frequency droop behavior to enable accurate power sharing between DGs. Frequency restoration is promptly initiated and completed within 0.6 s. The DGs' power and current responses are smooth, ripple-free, and free of overshoot in both cases.

These results demonstrate that PB-IMPC guarantees optimal control performance comparable to conventional MPC, while significantly reducing the computational burden. This efficiency gain enables the integration of additional functionalities, such as sensor fault tolerance, adaptive control, or multiobjective optimization, without increasing the overall control complexity or processing demands. Thus, PB-IMPC offers a more scalable and cost-effective solution for real-time inverter control in microgrids.

The average computational times of the IMPC and state observer were measured over 1000 cycles, yielding $t_{\text{IMPC}} = 1.2\,\mu s$ and $t_{\text{state-observer}} = 1.16\,\mu s$, respectively. The total computational time for the combined algorithm is $t_{\text{total}} = 2.36\,\mu s$. Compared to the conventional MPC, which required $t_{\text{MPC}} = 8.6\,\mu s$, the proposed IMPC reduces the computational burden by approximately 3.5 times.

VII. Conclusion

This article proposed a novel control strategy for GFM inverters that integrates passivity-based design with IMPC. The proposed approach reduces sensing requirements while maintaining high control performance, hence simplifying system design, enhancing its reliability, and lowering the overall cost.

Experimental results carried out in a two-DG microgrid demonstrated that the proposed controller maintains excellent performance even when any one group of sensors is removed, such as the capacitor voltage, output voltage, or output current. Under these sensorless conditions, the system continues to exhibit stable operation, accurate current control, effective voltage regulation, and proper power sharing, closely replicating the performance of the fully sensored configuration.

However, when input current measurements are removed, although the system remains operational, current quality deteriorates and power sharing becomes inaccurate. Nevertheless, the ability to sustain operation under such conditions highlights the fault-tolerant nature of the proposed controller, making it particularly valuable for mission-critical or remote applications where sensor failures may occur.

Overall, the proposed method provides a robust, computationally efficient, and cost-effective solution for GFM inverter control.

References

[1] K. Ma, S. Xia, Y. Qi, X. Cai, Y. Song, and F. Blaabjerg, "Power-electronics-based mission profile emulation and test for electric machine drive system—Concepts, features, and challenges," *IEEE Trans. Power Electron.*, vol. 37, no. 7, pp. 8526–8542, Jul. 2022.

[2] Y. Yang, Y. Wen, Z. Zhang, Y. Dong, C. Shen, and Y. Liu, "Toward 100% renewable power grids: A review," *IEEE Access*, vol. 13, pp. 69690–69704, 2025.

[3] F. Carnielutti, T. D. C. Busarello, Ê. C. Resende, Q. Ullah, and M. G. Simões, "Fixed switching frequency model predictive control for grid-forming inverters," *IEEE Trans. Power Electron.*, vol. 40, no. 7, pp. 9080–9089, Jul. 2025.

[4] N. Mohammed, H. Udawatte, W. Zhou, D. J. Hill, and B. Bahrani, "Grid-forming inverters: A comparative study of different control strategies in frequency and time domains," *IEEE Open J. Ind. Electron. Soc.*, vol. 5, pp. 185–214, 2024.

[5] R. Musca, E. R. Sanseverino, G. Zizzo, G. Giannuzzi, and C. Pisani, "Wide-synchronization control for power systems with grid-forming converters," *IEEE Trans. Power Syst.*, vol. 39, no. 3, pp. 4998–5007, May 2024.

[6] X. He, L. Huang, I. Subotić, V. Häberle, and F. Dörfler, "Quantitative stability conditions for grid-forming converters with complex droop control," *IEEE Trans. Power Electron.*, vol. 39, no. 9, pp. 10834–10852, Sep. 2024.

[7] B. Long, Y. Liao, K. T. Chong, J. Rodrıǵuez, and J. M. Guerrero, "Enhancement of frequency regulation in ac microgrid: A fuzzy-mpc controlled virtual synchronous generator," *IEEE Trans. Smart Grid*, vol. 12, no. 4, pp. 3138–3149, Jul. 2021.

[8] H. Zhang, C. Xue, R. Liu, and Y. Li, "Model-predictive dual-control loop with improved current-limiting capability for grid-forming inverter under grid faults," *IEEE Trans. Power Electron.*, vol. 40, no. 1, pp. 813–827, Jan. 2025.

[9] M. S. Ansari, S. Ahmad, and M. F. Azeem, "Performance analysis of PI and MPC controllers for grid-connected system," in *Proc. Int. Conf. Signal, Mach., Autom., Algorithm*. Springer, 2023, pp. 653–665.

[10] S. Samanta, N. R. Chaudhuri, and C. M. Lagoa, "Fast frequency support from grid-forming converters under dc- and ac-side current limits," *IEEE Trans. Power Syst.*, vol. 38, no. 4, pp. 3528–3542, Jul. 2023.

[11] M. Gursoy and B. Mirafzal, "Direct vs. indirect control schemes for grid-forming inverters–Unveiling a performance comparison in a microgrid," *IEEE Access*, vol. 11, pp. 75023–75036, 2023.

[12] C. Shen, W. Gu, X. Shen, and Y. Xu, "Lyapunov method-based coherent aggregation of grid-forming converters for transient stability equivalents," *IEEE Trans. Smart Grid*, vol. 16, no. 2, pp. 1462–1479, Mar. 2025.

[13] M. Li, E. Liu, H. Geng, Y. Mao, X. Wang, and X. Zhang, "Passivity-based control for the stability of grid-forming multi-inverter power stations," *IEEE Trans. Ind. Electron.*, vol. 72, no. 9, pp. 9117–9127, Sep. 2025.

[14] M. Ahmed, F. Alsokhiry, A. S. Abdel-Khalik, K. H. Ahmed, and Y. Al-Turki, "Improved damping control method for grid-forming converters using LQR and optimally weighted feedback control loops," *IEEE Access*, vol. 9, pp. 87484–87500, 2021.

[15] O. Babayomi, Y. Li, Z. Zhang, and K.-B. Park, "Advanced control of grid-connected microgrids: Challenges, advances, and trends," *IEEE Trans. Power Electron.*, vol. 40, no. 6, pp. 7681–7708, Jun. 2025.

[16] Z. Zhang, D. Sun, C. Zhao, Z. Gu, and H. Nian, "Enhanced grid-forming control strategy for DFIG participating in primary frequency regulation based on double-layer MPC in microgrid," *IEEE Trans. Energy Convers.*, vol. 40, no. 3, pp. 2679–2693, Sep. 2025.

[17] F. Carnielutti, M. Aly, M. Norambuena, J. Hu, J. Guerrero, and J. Rodriguez, "A master-slave model predictive control approach for microgrids," *IEEE Trans. Power Electron.*, vol. 40, no. 1, pp. 540–550, Jan. 2025.

[18] L. Guo and Y. Jia, "Inverse model predictive control (IMPC) based modeling and prediction of human-driven vehicles in mixed traffic," *IEEE Trans. Intell. Veh.*, vol. 6, no. 3, pp. 501–512, Sep. 2021.

[19] A. Ramadan, J. Choi, C. J. Radcliffe, J. M. Popovich, and N. P. Reeves, "Inferring control intent during seated balance using inverse model predictive control," *IEEE Robot. Autom. Lett.*, vol. 4, no. 2, pp. 224–230, Apr. 2019.

[20] A. Sharida, S. Bayhan, H. Abu-Rub, and U. Fesli, "Inverse model predictive control for power electronic converters," *IEEE Access*, vol. 12, pp. 68485–68496, 2024.

[21] A. Sharida, A. B. Bayindir, S. Bayhan, and H. Abu-Rub, "Enhanced inverse model predictive control for EV chargers: Solution for rectifier-side," *IEEE Open J. Ind. Electron. Soc.*, vol. 5, pp. 795–806, 2024.

[22] A. B. Bayindir, A. Sharida, S. Bayhan, and H. Abu-Rub, "Enhanced inverse model predictive control for EV chargers: Solution for dc–dc side," *IEEE Open J. Ind. Electron. Soc.*, vol. 6, pp. 478–490, 2025.

[23] A. Sharida, A. B. Bayindir, S. Bayhan, and H. Abu-Rub, "Inverse model predictive control for multi-port solid state transformer," in *Proc. IEEE 19th Int. Conf. Compat., Power Electron. Power Eng.*, 2025, pp. 1–6.

[24] X. Zhao and J. Zhao, "A robust and reduced-order power system dynamic state estimator for grid-forming inverters," *IEEE Trans. Instrum. Meas.*, vol. 74, 2025, Art. no. 9005312.

[25] A. Moulichon et al., "Observer-based current controller for virtual synchronous generator in presence of unknown and unpredictable loads," *IEEE Trans. Power Electron.*, vol. 36, no. 2, pp. 1708–1716, Feb. 2021.

[26] A. M. Akwasi, H. Chen, and J. Liu, "Grid forming inverters using reduced order-based Luenberger observer for power control," *Elect. Power Syst. Res.*, vol. 241, 2025, Art. no. 111424.

[27] F. Jukić, L. Pravica, M. Kovačić, and S. Stipetić, "Voltage sensorless synchronization of a grid-side converter based on a discontinuous operating mode and a sliding mode observer," *IEEE Trans. Ind. Appl.*, vol. 60, no. 4, pp. 6314–6325, Jul.–Aug. 2024.

[28] I. Poonahela et al., "Hierarchical model-predictive droop control for voltage and frequency restoration in ac microgrids," *IEEE Open J. Ind. Electron. Soc.*, vol. 4, pp. 85–97, 2023.
[29] B. Long, Z. Zhu, W. Yang, K. T. Chong, J. Rodrıǵuez, and J. M. Guerrero, "Gradient descent optimization based parameter identification for FCS-MPC control of LCL-type grid connected converter," *IEEE Trans. Ind. Electron.*, vol. 69, no. 3, pp. 2631–2643, Mar. 2022.
[30] A. Sharida, N. F. Kamal, H. Alnuweiri, S. Bayhan, and H. Abu-Rub, "Digital-twin-based diagnosis and tolerant control of T-type three-level rectifiers," *IEEE Open J. Ind. Electron. Soc.*, vol. 4, pp. 230–241, 2023.
[31] N. Baeckeland, D. Chatterjee, M. Lu, B. Johnson, and G.-S. Seo, "Overcurrent limiting in grid-forming inverters: A comprehensive review and discussion," *IEEE Trans. Power Electron.*, vol. 39, no. 11, pp. 14493–14517, Nov. 2024.
[32] N. Guler, S. Bayhan, and H. Komurcugil, "Equal weighted cost function based weighting factor tuning method for model predictive control in power converters," *IET Power Electron.*, vol. 15, no. 3, pp. 203–215, 2022.
[33] J. Jang, D. Kim, and I. Kim, "Singularity handling for unbalanced three-phase transformers in Newton–Raphson power flow analyses using Moore–Penrose pseudo-inverse," *IEEE Access*, vol. 11, pp. 40657–40674, 2023.

Ali Sharida (Member, IEEE) received the B.E. and master's degrees in mechatronics engineering from Palestine Technical University, Tulkarm, Palestine, and Palestine Polytechnic University (PPU), Hebron, Palestine, in 2013 and 2020, respectively. He received the Ph.D. degree in electrical engineering from Texas A&M University, College Station, TX, USA, in 2024.

He is currently a Postdoctoral Fellow with Qatar Environment and Energy Research Institute, Doha, Qatar. His current research interests include systems identification, power converter control, seamless transition, inverse predictive control, dual-active bridge, multiport solid-state transformers, and fast EV chargers.

Ahmed Kouzou (Graduate Student Member, IEEE) received the bachelor's degree in electrical and electronic engineering and the master's degree in power engineering from the Institute of Electrical and Electronic Engineering, University of Boumerdes, Boumerdes, Algeria, in 2017 and 2019, respectively. He is currently working toward the Ph.D. degree in electrical engineering with the Department of Electrical and Computer Engineering, Texas A&M University, College Station, TX, USA.

His research interests include, but are not limited to, microgrids, weak grids, and the integration of renewable energy sources (RES) into the power grid.

Anas Karaki (Member, IEEE) received the B.Sc. and M.Sc. degrees in electrical and computer engineering from Texas A&M University, College Station, TX, USA, in 2016 and 2020, respectively, and the Ph.D. degree in sustainable energy from Hamad Bin Khalifa University (HBKU), Doha, Qatar, in 2024.

He is a Postdoctoral Fellow with Qatar Environment and Energy Research Institute, HBKU. His research interests include power converter control, renewable energy integration, predictive control, energy management, game theory, reinforcement learning, and energy trading.

Ugur Fesli (Member, IEEE) received the bachelor's degree in electrical engineering from Gazi University, Ankara, Turkey, in 2006, and the M.S. degree in electrical and electronics engineering from Zonguldak Karaelmas (Bülent Ecevit) University, Zonguldak, Turkey, in 2009. He is currently working toward the Ph.D. degree in power systems and power electronics with the Department of Energy Systems Engineering, Graduate School of Natural and Applied Sciences, Gazi University.

He has been working as a Lecturer with Gazi University since 2009. His research interests include field of power systems and power electronics.

Sertac Bayhan (Senior Member, IEEE) received the M.S. degree and the Ph.D. degree in electrical engineering from Gazi University, Ankara, Türkey in 2008 and 2012, respectively.

His academic career commenced at Gazi University in 2009, ascending from a Lecturer to a Full Professor by 2022. Currently, he holds a dual appointment as a Principal Scientist at Qatar Environment and Energy Research Institute (QEERI) and a Professor with Gazi University. His research is at the forefront of power electronics and their pivotal roles in advanced power systems, focusing on renewable energy integration and, electrified transportation. His influence in his field led to be a Chair of the IES Power Electronics Technical Committee between 2018 and 2021. He also was a Delegate of IEEE-IES Energy Cluster between 2021 and 2023. Furthermore, he was an Associate Editor for several IEEE journals, including TRANSACTIONS ON INDUSTRIAL ELECTRONICS, IEEE JOURNAL OF EMERGING AND SELECTED TOPICS IN INDUSTRIAL ELECTRONICS, IEEE OPEN JOURNAL OF THE INDUSTRIAL ELECTRONICS SOCIETY, and IEEE INDUSTRIAL ELECTRONICS TECHNOLOGY NEWS.

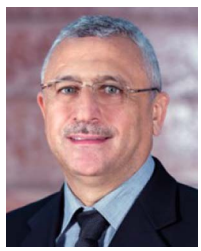

Haitham Abu-Rub (Fellow, IEEE) received the M.Sc. degree from Gdynia Maritime Academy, Gdynia, Poland, in 1990, and the Ph.D. degree from Technical University of Gdansk, Gdansk, Poland, in 1995, all in electrical engineering.

Since 2006, he has been with Texas A&M University at Qatar (TAMUQ), Doha, Qatar. For five years, he was the Chair for the electrical and computer engineering program at TAMUQ. He is currently a Professor with the College of Science and Engineering, Hamad Bin Khalifa University, Doha, Qatar. His main research interests are energy conversion systems, smart grid, renewable energy systems, electric drives, and power electronic converters.